AGU PUBLICATIONS

Paleoceanography

RESEARCH ARTICLE
10.1002/2014PA002736

Key Points:
- Amplitude modulation of axial obliquity controls the Late Cretaceous $\delta^{13}C$
- Transfer of the astronomical signal is examined with mass balance models
- Quasi-stable carbon reservoirs at middle to high latitudes provide the link

Supporting Information:
- Texts S1 and S2, Figures S1–S4, and Tables S1–S3

Correspondence to:
J. Laurin,
laurin@ig.cas.cz

Citation:
Laurin, J., S. R. Meyers, D. Uličný, I. Jarvis, and B. B. Sageman (2015), Axial obliquity control on the greenhouse carbon budget through middle- to high-latitude reservoirs, *Paleoceanography*, *30*, doi:10.1002/2014PA002736.

Received 9 OCT 2014
Accepted 19 JAN 2015
Accepted article online 26 JAN 2015

Axial obliquity control on the greenhouse carbon budget through middle- to high-latitude reservoirs

Jiří Laurin[1], Stephen R. Meyers[2], David Uličný[1], Ian Jarvis[3], and Bradley B. Sageman[4]

[1]Institute of Geophysics, Academy of Sciences of the Czech Republic, Prague, Czech Republic, [2]Department of Geoscience, University of Wisconsin-Madison, Madison, Wisconsin, USA, [3]School of Geography, Geology and Environment, Kingston University London, Kingston upon Thames, UK, [4]Department of Earth and Planetary Sciences, Northwestern University, Evanston, Illinois, USA

Abstract Carbon sources and sinks are key components of the climate feedback system, yet their response to external forcing remains poorly constrained, particularly for past greenhouse climates. Carbon-isotope data indicate systematic, million-year-scale transfers of carbon between surface reservoirs during and immediately after the Late Cretaceous thermal maximum (peaking in the Cenomanian-Turonian, circa 97–91 million years, Myr, ago). Here we calibrate Albian to Campanian (108–72 Myr ago) high-resolution carbon isotope records with a refined chronology and demonstrate how net transfers between reservoirs are plausibly controlled by ~1 Myr changes in the amplitude of axial obliquity. The amplitude-modulating terms are absent from the frequency domain representation of insolation series and require a nonlinear, cumulative mechanism to become expressed in power spectra of isotope time series. Mass balance modeling suggests that the residence time of carbon in the ocean-atmosphere system is—by itself—insufficient to explain the Myr-scale variability. It is proposed that the astronomical control was imparted by a transient storage of organic matter or methane in quasi-stable reservoirs (wetlands, soils, marginal zones of marine euxinic strata, and potentially permafrost) that responded nonlinearly to obliquity-driven changes in high-latitude insolation and/or meridional insolation gradients. While these reservoirs are probably underrepresented in the geological record due to their quasi-stable character, they might have provided an important control on the dynamics and stability of the greenhouse climate.

1. Introduction

The Late Cretaceous thermal maximum (Figure 1) stands out as a prime example of greenhouse climate attributed to high partial pressure of atmospheric carbon dioxide (pCO_2 800–1500 parts per million by volume, ppmv; [*Berner*, 2006]) and other greenhouse gases [*Beerling et al.*, 2011]. This interval provides a rare opportunity to examine the impact of primary climatic forcing such as quasi-periodic variations in insolation on the internal climatic mechanisms under extreme climatic conditions. Integral parts of the climate system are atmospheric, oceanic, and terrestrial carbon reservoirs, whose capacity and rates of carbon exchange control, among others, the radiative forcing from greenhouse gases. Because biotic processes involved in carbon exchange are associated with a differential uptake (fractionation) of the stable carbon isotopes (^{12}C and ^{13}C), the varying proportions of these isotopes in biogenic carbonates ($\delta^{13}C_{carb}$) and organic matter ($\delta^{13}C_{org}$) provide valuable tracers with which to study the interplay of the past carbon cycle and climate.

Unlike carbon-isotope records of other greenhouse and incipient icehouse intervals, which exhibit a strong astronomical control mostly in the 405 thousand year (kyr) eccentricity band [*Cramer et al.*, 2003; *Pälike et al.*, 2006; *Giorgioni et al.*, 2012], the Late Cretaceous carbon-isotope record appears notably weak in its astronomical signature. A potential record of the 405 kyr eccentricity cycle has been interpreted in parts of the Late Cretaceous [*Voigt et al.*, 2007; *Batenburg et al.*, 2012; *Sprovieri et al.*, 2013; *Laurin et al.*, 2014; *Paillard and Donnadieu*, 2014] (Figure 1), but it is generally small in magnitude. Most of the variance in the Cenomanian through Santonian carbon-isotope record occurs on a million year (Myr) scale (Figure 1; see also Figure S1 in the supporting information). Carbon-isotope excursions of up to 2‰ (4‰ including the Oceanic Anoxic Event II, OAE II; Figure 1) suggest systematic carbon transfers in the order of thousands of petagrams ($Pg = 10^{15}$ g; see Text S1 in the supporting information). These amounts are not particularly large compared to the major carbon isotope perturbations of the Cenozoic [*Zachos et al.*, 2001, 2008; *Cramer et al.*, 2009; *Friedrich et al.*, 2012], but they stand out as being particularly stable, recurring for over 15 Myr (Figure 1). Parts

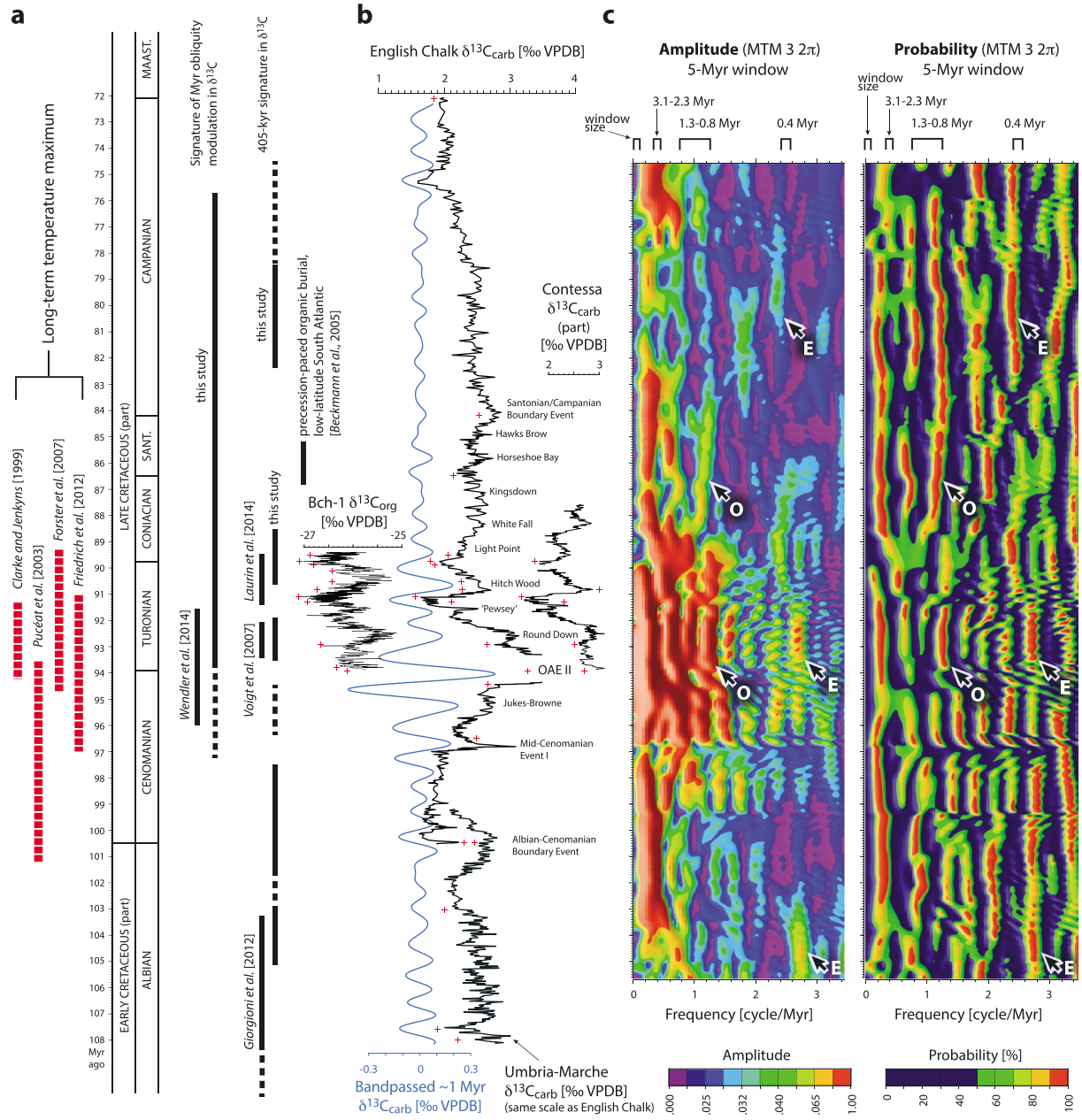

Figure 1. (a) Chronology of the Late Cretaceous thermal maximum. Data from *Clarke and Jenkyns* [1999], *Pucéat et al.* [2003], *Forster et al.* [2007], and *Friedrich et al.* [2012]. (b) Selected $\delta^{13}C$ data, calibrated in the time domain (crosses indicate age control points; Table 1). Bch-1: Bohemian Cretaceous Basin, central Europe [*Uličný et al.*, 2014]; English Chalk: Anglo-Paris Basin [*Jarvis et al.*, 2006]; Umbria-Marche: Central Apennines, Italy [*Giorgioni*, 2012; *Giorgioni et al.*, 2012]; Contessa: Central Apennines, Italy [*Stoll and Schrag*, 2000], Cenomanian data not shown. Previously interpreted orbital signatures are indicated. Blue curve is a band passed ~1 Myr (0.9 ± 0.3 cycle/Myr, Gaussian) component in the English Chalk $\delta^{13}C_{carb}$. Major positive carbon isotope events (CIEs) are labeled. (c) EHA spectral estimate for the recalibrated English Chalk $\delta^{13}C_{carb}$ curve stacked with the Umbria-Marche $\delta^{13}C_{carb}$ (Umbria-Marche $\delta^{13}C_{carb}$ data were modified by substracting 0.35‰, and attached to the English Chalk $\delta^{13}C_{carb}$ at the Albian/Cenomanian boundary). Traces of the potential obliquity amplitude modulation signal (O) and ~405 kyr eccentricity signal (E) are shown by arrows.

of this long-term variability have been attributed to the ~1.2 Myr cycle in amplitude modulation (AM) of Earth's axial obliquity [*Wendler et al.*, 2014] and multi-Myr modulation of orbital eccentricity [*Sprovieri et al.*, 2013]. Advances in radioisotopic dating [*Sageman et al.*, 2014], its integration with carbon-isotope stratigraphy [*Joo and Sageman*, 2014], and astrochronology independent of $\delta^{13}C$ data [*Laurin et al.*, 2014; *Ma et al.*, 2014] make it possible to test and refine these interpretations. In this paper, the hypothesis of a Myr-scale astronomical control is revisited, with a critical assessment using recently acquired, high-resolution $\delta^{13}C_{org}$ data (Bch-1 borehole, Figure S2 in the supporting information) [*Uličný et al.*, 2014]) and an updated chronology of the Late Cretaceous

Table 1. List of Age Control Points Used for the Age Calibration of $\delta^{13}C$ Data[a]

Stratigraphic Level	Age (Myr ago)	Uncertainty (Myr)	Source of Chronology
Base Maastrichtian	72.1	±0.2	*Ogg and Hinnov* [2012]
Base Campanian[b]	84.19	±0.38	*Sageman et al.* [2014]
Base Santonian[c]	86.49	±0.44	*Sageman et al.* [2014]
Base *C. crassus crassus* Zone	89.50	±0.06[g] (±0.38)[h]	*Laurin et al.* [2014] anchored to base Coniacian [*Sageman et al.*, 2014]
Base Coniacian[d]	89.75	±0.38	*Sageman et al.* [2014]
Didymotis Event I	89.89	±0.05[g] (±0.38)[h]	*Laurin et al.* [2014] anchored to base Coniacian [*Sageman et al.*, 2014]
Base *P. germari* Zone	90.13	±0.04[g] (±0.38)[h]	*Laurin et al.* [2014] anchored to base Coniacian [*Sageman et al.*, 2014]
Base *M. scupini* Zone	90.55	±0.05[g] (±0.38)[h]	*Laurin et al.* [2014] anchored to base Coniacian [*Sageman et al.*, 2014]
Peak Hitch Wood CIE[e]	90.84	±0.08[g] (±0.38)[h]	*Laurin et al.* [2014] anchored to base Coniacian [*Sageman et al.*, 2014]
Bridgewick CIE	91.11	±0.14[g] (±0.38)[h]	*Laurin et al.* [2014] anchored to base Coniacian [*Sageman et al.*, 2014]
Base *I. perplexus* Zone[f]	91.31	±0.07[g] (±0.38)[h]	*Laurin et al.* [2014] anchored to base Coniacian [*Sageman et al.*, 2014]
Base *C. woollgari* Zone	92.90	±0.15[h]	*Ogg and Hinnov* [2012]
Base Turonian	93.90	±0.15	*Meyers et al.* [2012a]; *Ogg and Hinnov* [2012]
OAE II, onset positive CIE	94.44	±0.02[g] (±0.15)[h]	*Sageman et al.* [2006]; *Meyers et al.* [2012a]; *Ma et al.* [2014]
Top Mid-Cenomanian Event I	96.5	n.d.	timing relative to base OAE II after *Lanci et al.* [2010]; cf. *Mitchell et al.* [2008]
Base Cenomanian	100.5	±0.4	*Ogg and Hinnov* [2012]

[a]For additional details, see Tables S1.1 through S1.7 in the supporting information.
[b]Correlated above peak "b" of the Santonian/Campanian Boundary CIE [*Jarvis et al.*, 2006; *Wendler*, 2013; *Joo and Sageman*, 2014].
[c]Correlated along the Michel Dean CIE [*Jarvis et al.*, 2006; *Wendler*, 2013; *Joo and Sageman*, 2014].
[d]Base C. *deformis erectus* Zone, approximates top Navigation CIE [*Walaszczyk et al.*, 2010; *Uličný et al.*, 2014].
[e]Hitch Wood I of *Uličný et al.* [2014].
[f]Coeval with the top of the Lower Southerham CIE [*Walaszczyk et al.*, 2010; *Uličný et al.*, 2014].
[g]Uncertainty of the floating astronomical time scale.
[h]Uncertainty applied from the nearest stage boundary.

[*Meyers et al.*, 2012a; *Ogg and Hinnov*, 2012; *Laurin et al.*, 2014; *Ma et al.*, 2014; *Sageman et al.*, 2014]. Our results furnish new arguments for the hypothesized dominance of obliquity modulation in carbon-isotope time series [*Wendler et al.*, 2014] and suggest that this pattern extended to the Campanian (Figure 1).

The task of identifying mechanisms that could develop prominent climate variations from the astronomical modulation terms while keeping a relatively low power at the primary orbital frequencies (i.e., precession and obliquity) is analogous to the "100 kyr problem" of the Late Pleistocene [*Imbrie et al.*, 1993]. The frequencies at which the precessional index and obliquity are modulated in their amplitude are extremely weak or absent from the frequency spectra of insolation series [*Berger et al.*, 1993; *Laskar et al.*, 1993] and require a nonlinear mechanism (e.g., "memory") to develop a discrete cycle in a paleoclimate proxy [*Short et al.*, 1991; *Beaufort*, 1994; *Herbert*, 1997; *Cramer et al.*, 2003; *Pälike et al.*, 2006]. The residence time of carbon in the ocean (~100 kyr) [*Kump and Arthur*, 1999] has been cited as a carrier of this "memory", and has been used to explain carbon-isotope cyclicity at the 405 kyr eccentricity scale [*Cramer et al.*, 2003; *Pälike et al.*, 2006]. As shown below, however, the ability of residence time to amplify Myr-scale modulation terms is very limited. In the second part of this paper it is argued that this pattern of carbon-isotope variability likely reflects obliquity-paced buildup and decay of terrestrial or marine carbon reservoirs at high to middle latitudes.

2. Methods

2.1. Age Calibration of $\delta^{13}C$ Data

Published $\delta^{13}C_{org}$ and $\delta^{13}C_{carb}$ data from several key localities were anchored to the Late Cretaceous chronology [*Meyers et al.*, 2012a; *Ogg and Hinnov*, 2012; *Laurin et al.*, 2014; *Sageman et al.*, 2014] using 10 to

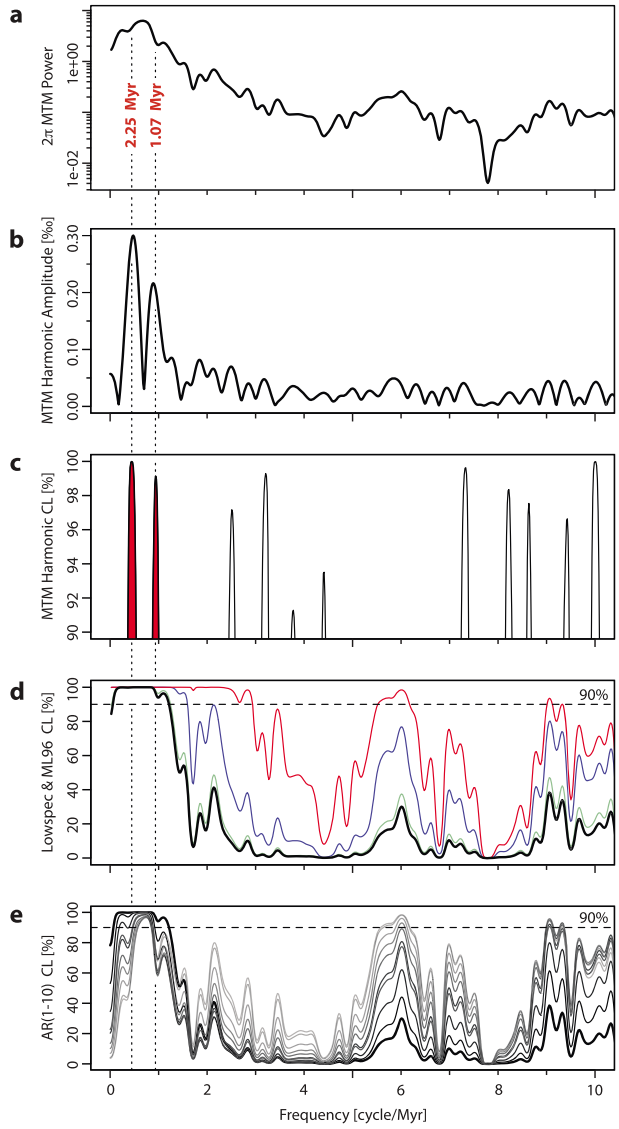

Figure 2. Bch-1 $\delta^{13}C_{org}$ spectral analysis and noise model evaluation. (a) The 3–2π MTM power spectrum. (b) The 3–2π MTM harmonic amplitudes. (c) The 3–2π MTM harmonic *F* test confidence levels. (d) Classic AR(1) model confidence levels (black bold line), and various "robust" estimates, including: ML96 method (red), modified ML96 method (green), and LOWSPEC (blue). (e) Evaluation of all AR noise models from AR(1) to AR(10) (see section 2). The AR1 model is shown as a bold black line, while the lighter lines indicate successively more complex models (lightest gray is AR(10)).

16 biostratigraphic and carbon-isotope markers (Table 1; for details, see Tables S1.1–S1.7 in the supporting information). Importantly, although the ages of many of these markers incorporate astronomical constraints, the long-period obliquity modulations examined in the present study were not directly employed in prior chronology work. Linear sedimentation rates were applied between the 10 and 16 age control points. This approach provides age calibration independent of any interpretation of a long-period obliquity signature in the carbon-isotope record, thus reducing the risk of a circular argument.

All carbon-isotope values are reported in a standard delta (δ) notation as per mil (‰) relative to the Vienna Peedee belemnite standard.

2.2. Time Series Analysis

Spectral estimates are calculated with the multitaper method (MTM) [*Thomson*, 1982] using the R package "astrochron" [*S. R. Meyers*, 2014]. A number of complementary approaches are applied, including MTM power spectral analysis, MTM harmonic analysis (amplitude), and evolutive harmonic analysis [*Meyers et al.*, 2001]. To quantify the statistical significance of the Bch-1 spectral results, we use the MTM harmonic *F* test (for phase-coherent sinusoids; [*Thomson*, 1982]), and the Bch-1 power spectrum is also evaluated against a wide range of potential red noise hypotheses (Figure 2). Unless otherwise indicated, all analyses use three tapers and a time-bandwidth product of 2, and the data are linearly detrended prior to analysis.

In total, 13 different red noise models are developed to address well-known challenges and pitfalls in the interpretation of low-frequency paleoclimate variability [*Mann and Lees*, 1996; *Wunsch*, 2010; *Meyers*, 2012]. This comprehensive approach is essential in the present study, given our focus on hypothesized low-frequency astronomical cycles that can be difficult to detect with some statistical testing methods but can also be artificially generated by other approaches [*Meyers*, 2012]. The specific red noise models used here include the conventional AR(1) model [*Gilman et al.*, 1963], three different "robust" AR(1) models (ML96, modified ML96, and LOWSPEC [*Mann and Lees*, 1996; *Meyers*, 2012]), and higher-order autoregressive noise models spanning AR(2) to AR(10) [*Percival and Walden*, 1998] (Figure 2). The ML96 approaches employ a 20% median smoothing window and an analytic fit to log-transformed power. The "modified" ML96 approach implements Tukey's robust end-point rule [*Tukey*, 1977] to help overcome undesirable "edge effects"

associated with the standard ML96 approach, which can artificially generate significant low-frequency cycles [*Meyers*, 2012].

Coherency estimates are based on the Blackman-Tukey method [*Blackman and Tukey*, 1958] using a Bartlett window and autocovariance calculated on 50% of the data series (Analyseries software [*Paillard et al*., 1996]). Obliquity AM envelopes were obtained with the Hilbert transform in "astrochron" [*S. R. Meyers*, 2014].

Preparation of the Bch-1 $\delta^{13}C_{org}$ data involved resampling on an evenly spaced grid by piecewise linear interpolation. Overinterpolation is an issue of particular concern for the evaluation of red noise models [*Mudelsee*, 2010]. The present study uses a 7 kyr interpolation grid; approximately 91% of the data and 73% of the total interval duration have a sample resolution that is finer than this value. The English Chalk $\delta^{13}C_{carb}$ record was resampled on a 5 kyr grid; this relatively fine-scale grid is acceptable for the evolutive harmonic analysis (Figure 1), given the caveat that we restrict our analysis to long-period terms (≥250 kyr). The Bch-1, La04, La10a, and La10d data were zero padded to 9000 points.

2.3. Theoretical Astronomical Solutions

Obliquity and precession index for the La10a–La10d solutions [*Laskar et al*., 2011] were computed following the procedure described in *Wu et al*. [2013]. Analyseries [*Paillard et al*., 1996] provided orbital parameters for the solution La04 [*Laskar et al*., 2004]. We note that all available solutions are unstable beyond 50 Ma [*Laskar et al*., 2011]. The La04 and La10a–La10d series are therefore used only as examples of the potential variability of astronomical parameters in the study interval.

2.4. Isotopic Mass Balance Models

Two groups of isotopic mass balance models were used to examine the possible pathways of astronomical control on Myr-scale signatures in $\delta^{13}C$. The model parameters are described below.

2.4.1. Gradual Response Models (GO, GM, and GC)

This group of models makes it possible to analyze the effect of carbon residence time on the transfer of variance from the primary astronomical wavelengths (~20 kyr precession or ~40 kyr obliquity) to the wavelengths at which the amplitudes of the precessional and obliquity signals are modulated. Here we assume that net carbon burial fluxes respond proportionally to clipped obliquity forcing (see below).

The carbon-isotope composition of the exogenic carbon reservoir ($\delta^{13}C_0$) is calculated as a function of carbon input from volcanogenic, metamorphic and weathering sources (in sum designated as F_{in}), and net burial fluxes of bulk organic carbon (F_{org}), carbonate carbon (F_{carb}), and biogenic methane carbon (F_{meth}), all of which are relative to the molar size of the exogenic reservoir (M_0):

$$d\delta^{13}C_0/dt = \left(F_{in}\delta^{13}C_{in} - F_{org}\delta^{13}C_{org} - F_{carb}\delta^{13}C_{carb} - F_{meth}\delta^{13}C_{meth}\right)/M_0 \quad (1)$$

where

$$\delta^{13}C_{org} = \delta^{13}C_0 + \varepsilon_{org} \quad (2)$$

$$\delta^{13}C_{carb} = \delta^{13}C_0 + \varepsilon_{carb} \quad (3)$$

$$\delta^{13}C_{meth} = \delta^{13}C_0 + \varepsilon_{meth} \quad (4)$$

The isotopic composition of carbon input ($\delta^{13}C_{in}$) is set at −4‰ (based on the proportions of volcanogenic, metamorphic, organic-weathering, silicate-weathering, and carbonate-weathering carbon sources as in *Kump* [1991] and *Kump and Arthur* [1999]). We employ fixed fractionation factors of −28‰ for bulk organic carbon (ε_{org}), +2‰ for carbonate carbon (ε_{carb}), and −60‰ for biogenic methane carbon (ε_{meth}). Values at the upper limits of published fractionation factors [*Hayes et al*., 1999; *Kump and Arthur*, 1999; *Dickens*, 2003; *P. A. Meyers*, 2014] maximize the isotopic effect of burial fluxes and thus help to delineate the maximum efficiency of carbon residence times in amplifying the Myr-scale variance in $\delta^{13}C_0$. The role of changing isotopic composition and mass of authigenic carbonates [*Schrag et al*., 2013] is not explicitly modeled. The fractionation factors of this carbon sink are highly variable depending on the sources of alkalinity [e.g., *Anderson et al*., 1987; *Roberts and Aharon*, 1994; *Reimers et al*., 1996; *Meister et al*., 2007; *Naehr et al*., 2007; *O'Reilly et al*., 2014]. Authigenic carbonate formation could be responsible for local or regional differences in the $\delta^{13}C_{carb}$ signatures and might have particularly affected $\delta^{13}C_0$ during intervals of widespread anoxia

(e.g., OAE II; cf. *Schrag et al*. [2013]). The globally consistent $\delta^{13}C_{carb}$ signatures of major carbon isotope events (CIEs) covering a range of paleogeographic, depositional, and diagenetic settings (review in *Wendler* [2013]), however, suggest that either the bulk of authigenic carbonate was similar in its carbon-isotope composition to biogenic carbonate precipitates (and can be approximated by $\delta^{13}C_{carb}$ in equation (1)), or the mass was negligible on global scale. We acknowledge that a localized formation of a large mass of isotopically distinct authigenic carbonate remains possible (e.g., in parts of the Pacific or Arctic). This (unlikely) case, however, cannot be included in isotopic mass balance estimates unless carbon-isotope data from the particular reservoir are available.

The clipped obliquity forcing of net burial fluxes was obtained using a modified version of the nonlinear function of *Cramer et al*. [2003]:

$$F = d \times \{F_{min} + [\exp((-o' - a)/b) + c] \times [F_{max} - F_{min}]\} \quad (5)$$

where

$$o' = (o - \bar{o})/1000 \quad (6)$$

Obliquity (o) was calculated using the La04 solution [*Laskar et al*., 2004]. The lower and upper limits of burial fluxes, F_{min} and F_{max}, are loosely constrained based on *Locklair et al*. [2011], who extrapolated local estimates of organic and inorganic burial fluxes from several sites and intervals to the entire surface area of the Cretaceous ocean. Methane burial fluxes are allowed to vary in the same range as the organic burial fluxes, because no comprehensive estimate of F_{meth} is available for the study interval. Equation (5) is always applied to one burial flux (F_{meth} in GM runs, F_{org} in GO runs, and F_{carb} in GC runs), while the other burial fluxes are kept constant. The ratio of weighted means of F_{carb} versus F_{org} is set at 4.2:1, similar to the ratios used in *Kump and Arthur* [1999] and *Kurtz et al*. [2003]. The mean ratio of F_{org} versus F_{meth} is set arbitrarily at 1.8:1 in the GM model runs. The multiplier d makes it possible to linearly adjust the burial fluxes and carbon residence times. Parameters a, b, and c control the amplitude, asymmetry, and minimum value of the obliquity-scale fluctuations, respectively. In all GO, GC, and GM experiments, the asymmetry is set to its maximum (equivalent to clipping at the mean obliquity level) in order to promote variance at the modulating frequencies (for an example of model input and output, see Figure S4.1 in the supporting information). The model parameters are presented in Table S2.1 in the supporting information.

2.4.2. Threshold Response Models

Models THM, THOt, and THCpr offer an alternative mode of transfer of the astronomical signal to the carbon-isotope record. These models assume a buildup of quasi-stable carbon reservoirs (R_q) of bulk organic carbon (models THOt), carbonate (THCpr) or biogenic methane (THM) when axial obliquity (o; models THM-OBL, THOt-OBL, and THCpr-OBL), or the precession index ($e \sin\varpi$; model THM-PREC) fall below a threshold (th1). Above th1 these reactive reservoirs remain stable until obliquity or the precession index reach a second threshold (th2). For $o >$ th2 or ($e \sin\varpi$) $>$ th2, the reactive reservoirs decay and the stored carbon is returned to the exogenic reservoir. Above th1 and below th2, the rates of R_q buildup or decay remain constant, i.e., not proportional to the orbital forcing. A reverse model setup (labeled rev) assumes buildup above th1 and decay below th2. All models employ equation (1) to calculate $\delta^{13}C_0$. Here a relatively low fractionation factor of −26‰ is used for the organic carbon R_q to account for a terrestrial component in the reservoir. Importantly, to facilitate the comparison of different model suites, the ratio of background burial fluxes F_{carb} versus F_{org} is the same as the ratio of mean burial fluxes used in the GC and GO models (for details, see Table S2.2 in the supporting information). Obliquity and precession index series were obtained with the solutions La04 [*Laskar et al*., 2004], La10a [*Laskar et al*., 2011], and La10d [*Laskar et al*., 2011] (see Table S2.2 in the supporting information).

3. Results and Discussion

3.1. A Record of Obliquity Modulation in the Turonian-Coniacian

Spectral estimates for age-calibrated $\delta^{13}C_{org}$ from borehole Bch-1 (Figure 1) reveal cycles at 2.25 Myr and 1.07 cycle/Myr that pass the 99% harmonic F test confidence level and surpass the 96% confidence level for a range of autoregressive red-noise models (Figures 2 and 3). A statistically less significant power and amplitude spectral maximum is found at 6 cycles/Myr (167 kyr wavelength). This feature does not reach

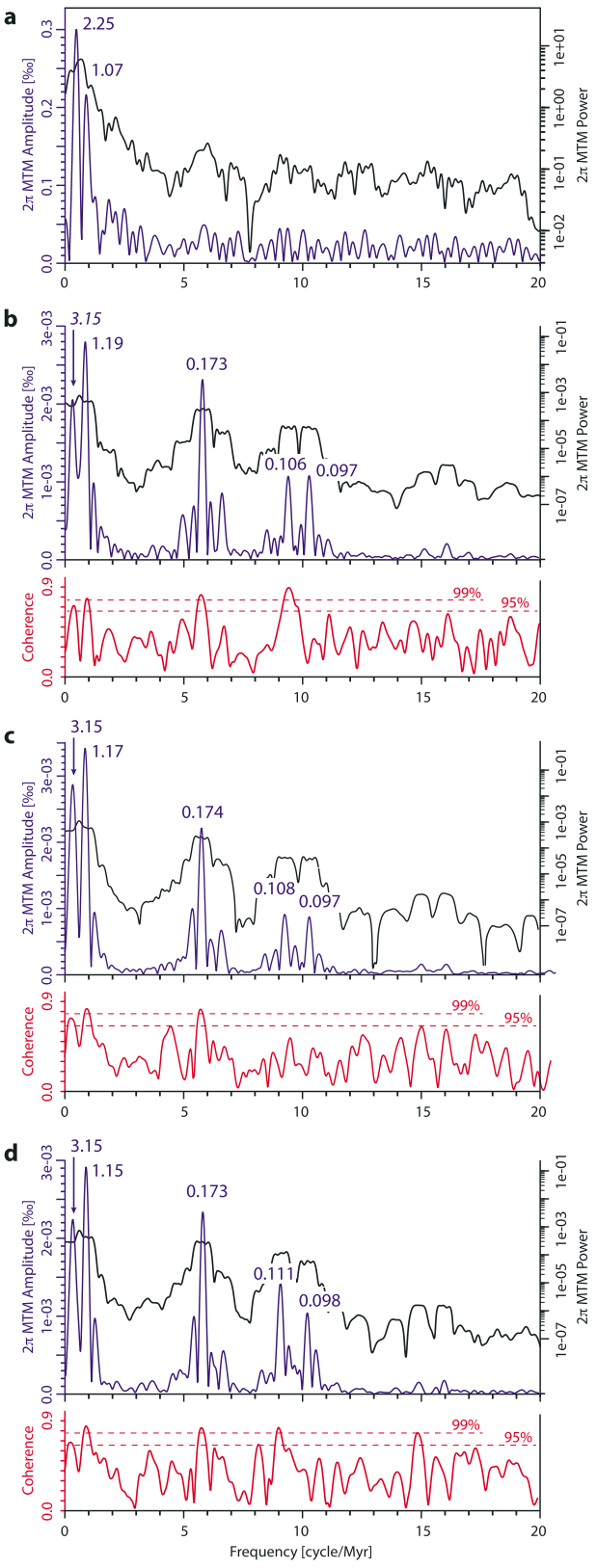

high *F* test confidence level scores in the bulk spectral estimate but is more significant in a subset of the investigated red noise models (Figure 2), and also forms a persistent trace (97–99% *F* test confidence level) in the Evolutive Harmonic Analysis (EHA) spectrogram of the middle part of the study interval (Figure 4). Cross-spectral analysis with AM envelopes of axial obliquity calculated with the available astronomical solutions [*Laskar et al.*, 2004, 2011] suggests nonzero coherency at >95% confidence level for wavelengths 2.38–3.13, 0.98–1.28, 0.17–0.18, and 0.11 Myr (Figure 3). Taken together, these analyses suggest that all major terms that modulate the amplitude of axial obliquity are present in the $\delta^{13}C_{org}$ series (the 3.15 Myr cycle observed in the amplitude spectra is slightly displaced, although it falls within the Rayleigh resolution; analysis of longer sections of the La10a and La10d solutions indicates a cycle of ~2.3 Myr). While ~2.5 and ~0.1 Myr components are also present in the spectrum of orbital eccentricity that modulates the precessional index, the other two components (~1 Myr and ~170 kyr) are unique to obliquity modulation. Below, it is demonstrated that the interplay of ~1 Myr and ~2.5 Myr variability in $\delta^{13}C$ can be reproduced solely by obliquity forcing. The most stable, 405 kyr, term of orbital eccentricity is apparent in parts of the study interval (e.g., Late Turonian) but appears as a low-amplitude, transient feature superimposed upon Myr-scale variability.

Figure 3. Selected spectral estimates for age-calibrated $\delta^{13}C_{org}$ (Bch-1 borehole) and obliquity amplitude envelopes (solutions La04, La10a, and La10d [*Laskar et al.*, 2004, 2011]). (a) Multitaper method (MTM) power (black) and amplitude (blue) spectral estimates for Bch-1 data. (b) MTM power (black), amplitude (blue) and Blackman-Tukey coherence (red) estimates for La04 obliquity AM. The 99% and 95% confidence levels for coherence relative to $\delta^{13}C_{org}$ are indicated. (c) and (d) Same as Figure 3b for the solutions La10a and La10d, respectively. Numbers denote wavelengths (in Myr) of spectral maxima that exceed the 90% *F* test confidence level (84.97% is italicized in Figure 3b).

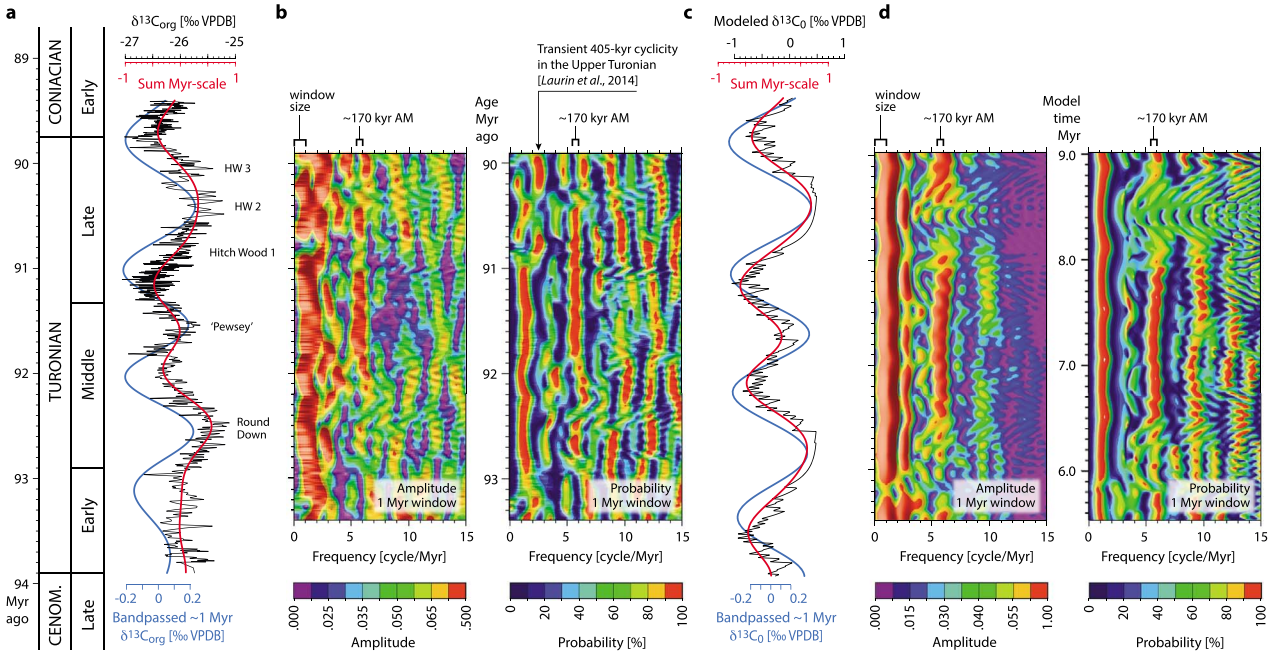

Figure 4. (a) Age-calibrated $\delta^{13}C_{org}$, Bch-1 borehole. Major CIEs indicated (HW2 and HW3 refer to Hitch Wood 2 and Hitch Wood 3 [*Uličný et al*., 2014]). Band passed ~1 Myr signal (Gaussian filter 0.9 ± 0.3 cycle/Myr) in blue and a sum of Myr-scale components (piecewise linear filter 0.7 ± 0.7 cycle/Myr) in red. The broader filter should be less sensitive to nonstationarities in the signal, and is therefore used as the target for isotopic mass balance simulations (Figure 5). (b) EHA spectral estimate for the calibrated Bch-1 curve. Note that the 405 kyr eccentricity signature interpreted earlier [*Laurin et al*., 2014] forms only a transient feature in the study interval. (c) The $\delta^{13}C_0$ simulated with obliquity-driven, quasi-stable reservoir model (THM-OBL-La04; "0" model time = 100 Myr ago in *Laskar et al*. [2004]; see Figure 6 and Table S2.2 in the supporting information). Band passed signals as in Figure 4a. (d) EHA spectral estimate for the simulated $\delta^{13}C_0$. Note the concentration of power at the ~170 kyr wavelength and its similarity with transient ~170 kyr signature in the calibrated Bch-1. Longer AM wavelengths are biased due to the size of the EHA window (1 Myr). For alternative solutions, see Figures S4.2–S4.12 in the supporting information.

The ~1 Myr variations are defined by transitions between major, globally recognized positive $\delta^{13}C$ excursions (the Round Down, "Pewsey", Hitch Wood, and Light Point CIEs of *Jarvis et al*. [2006]) and negative $\delta^{13}C$ anomalies (Lulworth, Glynde, Bridgewick, and Navigation CIEs; Figure 1). The detailed timing of these excursions is, however, often offset from maxima and minima in the band passed ~1 Myr cycle, suggesting that they record an interplay with other orders of cyclicity (both shorter and longer), or nonastronomical influences. All theoretical solutions for the obliquity series [*Laskar et al*., 2004, 2011] suggest a marked variability in a spacing of ~1 Myr maxima and minima in the AM envelope (Figure S3 in the supporting information). The range of apparent wavelengths can be further enhanced by nonlinear transformation of the obliquity signal: for example, mass balance models presented below produce wavelengths ranging from 0.68 to 1.55 Myr (Figures S4.1–S4.11 in the supporting information). In addition to these effects, the timing of some of the isotope peaks or troughs is likely influenced by changes in biogenic isotope fractionation due to changing pCO_2 or nutrient levels [*Kump and Arthur*, 1999], as indicated by the convergence of $\delta^{13}C_{org}$ and $\delta^{13}C_{carb}$ in the upper part of the Late Turonian Hitch Wood CIE (Figure 1). Hence, the above results generally support a previous interpretation that recognized the signature of obliquity modulation in the carbon-isotope record of the Lower and Middle Turonian [*Wendler et al*., 2014] but suggest that the individual maxima or minima in $\delta^{13}C$ are not strictly spaced by 1.2 Myr intervals.

It should be noted that the Bch-1 record spans ~4.5 Myr, while a robust statistical evaluation of Myr-scale cyclicity requires a longer time series. The long-term stability of the Myr-scale signature in $\delta^{13}C$ is therefore further explored below.

3.2. Long-Term Stability of the ~1 Myr Signature

EHA spectrogram of the English Chalk $\delta^{13}C_{carb}$ reference curve [*Jarvis et al*., 2006] recalibrated in the time domain (see section 2 and Table S1.2 in the supporting information) reveals a persistent, statistically significant (>90%) feature at 1.0–1.3 cycle/Myr (0.8–1.0 Myr wavelength) paralleled by a less continuous trace

at 0.6–0.9 cycle/Myr (1.1–1.7 Myr wavelength) in the Coniacian through Campanian (Figure 1c). This cyclicity involves globally recognized excursions such as the White Fall, Kingsdown, Horseshoe Bay, Hawks Brow, and the Santonian/Campanian Boundary CIEs [*Jarvis et al*., 2006]. The amplitude fades toward the Middle and Late Campanian (Figure 1) but possibly recurs in the Middle and Late Maastrichtian [*Batenburg et al*., 2012]. Toward older strata, the ~1 Myr feature reappears in the Lower and Middle Turonian, consistent with the Bch 1 results. The weak EHA response observed in the Late Turonian is attributable to the differences between $\delta^{13}C_{carb}$ and $\delta^{13}C_{org}$ that are probably related to biogenic fractionation effects (see above). The EHA spectral estimate does not reveal a persistent statistically significant ~1 Myr cycle in the Cenomanian, but a broadband (0.9 ± 0.3 cycle/Myr) filter of the calibrated $\delta^{13}C_{carb}$ curve reveals that the major excursions —OAE II, the Jukes-Browne CIE, and Mid-Cenomanian Event I (MCE I)—fit in the loosely defined ~1 Myr rhythm (Figure 1). This pattern supports the hypothesis that the detailed timing and structure of the carbon-cycle perturbation during OAE II were ultimately paced by insolation changes [*Mitchell et al*., 2008], however, in a setting preconditioned by volcanogenic supply of nutrients [*Snow et al*., 2005; *Turgeon and Creaser*, 2008]. The potential ~2.25 Myr rhythm identified in the Bch-1 data (Figures 2 and 3) is not an obvious persistent feature in the longer interval covered by English Chalk $\delta^{13}C_{carb}$ record. This nonstationarity possibly involves nonorbital influences (e.g., tectonically controlled changes in weathering rates and nutrient delivery) but may also be related to instabilities in the ~2.5 Myr AM observed in theoretical solutions (Figure S3 in the supporting information). The influence of eccentricity AM is another potential factor to consider on multi-Myr time scales [cf. *Boulila et al*., 2012; *Sprovieri et al*., 2013].

The obliquity-modulation signature in the carbon-isotope record has two important implications. First, it points to a distinct mode of transfer of the astronomical signal in a climate system that is capable of amplifying the modulating term. Second, because obliquity has a limited range of insolation effects, its dominance in $\delta^{13}C$ data points to a limited range of geographic locations and temporal (seasonal) intervals where the carbon sources and sinks responsible for the perturbations in carbon budget can be sought.

3.3. The Mechanism of AM Amplification

Astronomical insolation changes can apply their effect on the carbon-isotope composition of the exogenic carbon pool ($\delta^{13}C_0$) most efficiently via changes in the rates of the following: (1) production and burial, or remineralization, of organic matter; (2) precipitation and dissolution of carbonate; or (3) production and storage, or oxidation, of biogenic methane. These processes are either linked directly to changes in insolation or are controlled via a chain of mediating climatic and oceanographic mechanisms. The sources of the distinct, nonlinear response of the Late Cretaceous carbon-isotope record to orbital insolation must be contained in the nature of these causal links.

Sea level change is the obvious candidate for the AM amplification because its influence on marine and coastal sedimentation—and hence some of the major carbon and nutrient inventories—is inherently associated with deformation of amplitudes and phasing of the system's response to insolation [e.g., *Swenson*, 2005; *Laurin et al*., 2005]. In addition to the persisting controversy on the scales and origin of greenhouse eustasy [e.g., *MacLeod et al*., 2013; *Uličný et al*., 2014], however, none of the nonlinear mechanisms has been shown capable of transferring an appreciable amount of variance to the Myr-scale periods of AM. If the Late Cretaceous eustatic sea level change followed the same frequencies as the Myr modulation terms of eccentricity and obliquity (as suggested by *Boulila et al*. [2011] and *Wendler et al*. [2014]), it must have been a product, rather than source, of the mechanisms amplifying the AM component of insolation forcing. Other nonlinear processes described in the literature either provide only limited support for the Myr-scale variance [*Short et al*., 1991; *Herbert et al*., 1999] or act on time scales that greatly exceed the ~1 Myr cyclicity (e.g., self-sustaining oscillation in coupled phosphorus and oxygen cycles; [*Handoh and Lenton*, 2003]). A possible exception is the effect of long residence time of carbon in the exogenic reservoir.

The carbon residence time transfers some degree of variance from astronomical insolation periods (primarily those of the precessional index and obliquity, i.e., ~20 kyr and ~40 kyr) toward longer periods, namely, the 405 kyr eccentricity term [*Cramer et al*., 2003; *Pälike et al*., 2006]. Here isotopic mass balance simulations are performed to examine the ability of carbon residence time to support variance at longer Myr-scale periods. Changes in $\delta^{13}C_0$ are modeled with changing organic and inorganic carbon burial fluxes that respond proportionally to a clipped obliquity signal (models GO, GM, and GC; see section 2; Table S2.1 and Figure S4.1 in the supporting information). The results suggest that obliquity-driven changes in carbon

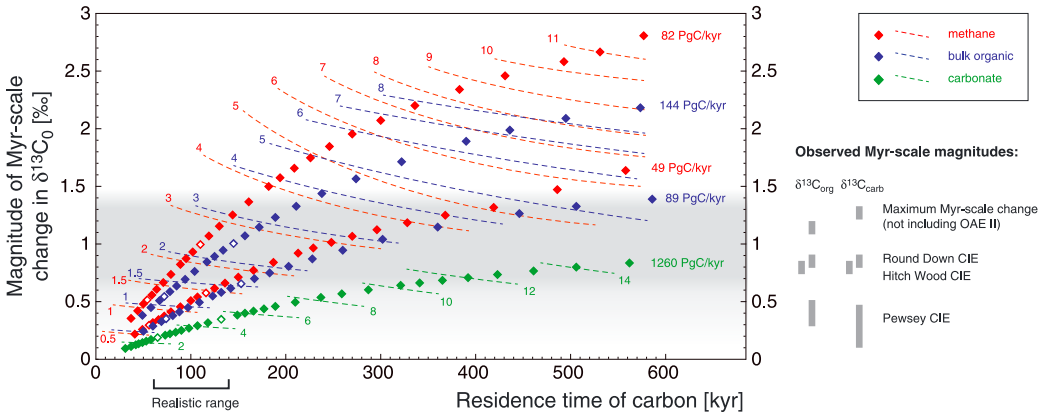

Figure 5. Model output illustrating the limitations of the carbon residence time in amplifying the Myr-scale component in obliquity-paced $\delta^{13}C_0$. Net burial fluxes of methane-carbon ($\varepsilon = -60‰$), bulk organic carbon ($\varepsilon = -28‰$), and carbonate carbon ($\varepsilon = +2‰$) were assumed to respond proportionally to a clipped obliquity forcing (models GO, GM, and GC; see section 2 and Table S2.1 in the supporting information). Data points (diamonds) represent the magnitudes of Myr-scale cycles in the $\delta^{13}C_0$ output (piecewise linear filter 0.7 ± 0.7 cycle/Myr) for given residence times. Dashed contours indicate the proportion of the maximum obliquity-scale magnitude in the net burial flux (constant for each series of models; indicated along the right margin) versus weighted mean of the same burial flux (red = methane carbon, blue = bulk organic carbon, and green = carbonate carbon). In order to transfer an appreciable amount of variance to the Myr-scale AM wavelengths, the model requires either an extremely long residence time of carbon or very large magnitudes of obliquity-scale variations in the net burial fluxes. Open diamonds denote model runs in which the mean burial fluxes are similar to the global burial fluxes as in *Kurtz et al.* [2003] (60 Pg/kyr for organic carbon and 242 Pg/kyr for carbonate carbon) and *Kump and Arthur* [1999] (120 Pg/kyr for organic carbon and 484 Pg/kyr for carbonate carbon). The observed magnitudes of Myr-scale change in $\delta^{13}C_{org}$ and $\delta^{13}C_{carb}$ (piecewise linear filter 0.7 ± 0.7 cycle/Myr) in the Turonian part of the study interval (borehole Bch-1 and English Chalk) are shown by vertical grey bars on the right. The range of maximum Myr-scale magnitudes in the available data is further highlighted by shading.

burial are capable of producing appreciable variability at the Myr-scale periods. However, even at the maximum asymmetry (i.e., zero sensitivity to the opposite phase of the obliquity forcing; see section 2), the model requires enormous variations in the short-term (obliquity-paced) global burial fluxes to reproduce a 1‰ $\delta^{13}C$ cycle at the Myr scale (Figure 5). The variations required here are several times higher than short-term variations estimated or modeled for parts of the Phanerozoic [e.g., *Arthur et al.*, 1988; *Louis-Schmid et al.*, 2007; *Toggweiler*, 2008; *Ma et al.*, 2011; *Donnadieu et al.*, 2011; *Tian et al.*, 2014]. Among other aspects, they would be associated with extreme nutrient demands to saturate biological productivity and would induce high-amplitude changes in pCO_2 over short time scales (incompatible with the available temperature-proxy data, e.g., *MacLeod et al.* [2013]). Similar limitations apply to precession- and eccentricity-driven changes in $\delta^{13}C_0$ [cf. *Laurin et al.*, 2014]. It is concluded that carbon burial proportional to (clipped) orbital insolation cannot alone explain the Myr-scale variability observed in the study interval. This claim is consistent with the output from more complex carbon cycle models [*Pälike et al.*, 2006] that produce well-defined cycles at the 405 kyr period but only minor variability at the Myr-scale AM wavelengths. In order to reduce the magnitude of short-term fluctuations and keep residence times of carbon in a realistic range, the $\delta^{13}C_0$ response to obliquity forcing must involve a more complex relationship. Below, we offer a solution that effectively reduces the short-term variability by introducing a nonlinear threshold behavior and carbon recycling on astronomical time scales. In these solutions, major changes in the net carbon burial fluxes are tied to a development and decay of new carbon sinks rather than to changes in the intensity of carbon production and efficiency of carbon burial in the existing carbon reservoirs.

The models cited above assume that, once buried, carbon is permanently (relative to the model time span) removed from the carbon cycle. More realistically, however, carbon burial proceeds via a series of reservoirs that are stable only under certain climatic and depositional conditions (cf. "rapid recycling" in *Berner* [1987, 2006] and *Berner and Canfield* [1989]; "capacitor" in *Dickens* [2003] and *Komar et al.* [2013]). Examples of such quasi-stable reservoirs include fluvial and lacustrine deposits, terrestrial and coastal peats and soils, methane hydrate reservoirs in deep marine sediments and permafrost, marine euxinic settings, and intermediate water carbonate deposits. Sediment accretion, compaction, and subsidence make it possible to transfer carbon

out of the reach of surface processes and reduce the carbon exchange with the exogenic pool. However, these reservoirs are also easily destabilized when depositional conditions change. Fluctuations in precipitation/evaporation balance in terrestrial environments, sea level in coastal settings, temperature in high-latitude zones of permafrost formation, rates of intermediate or deep water formation in euxinic settings, or carbonate saturation levels, are only a few examples of processes that can change the efficiency of carbon removal or even reconfigure a carbon sink to a net carbon source. The efficiency of carbon recycling depends on many factors including the structure of the reservoir, sediment accretion or erosion rates, and the types of carbon species buried. Data from Holocene soils, however, suggest that the amounts of reactive carbon and the rates of its recycling upon erosion can be substantial even in semiarid environments [*Marin-Spiotta et al*., 2014]. Extremely high outgassing rates can be expected from peat combustion upon aridization [*Turetsky et al*., 2015] and permafrost thaw (up to 1.5 Pg of carbon per year [*DeConto et al*., 2012]).

The potential role of buildup and decay of quasi-stable reservoirs on the structure of $\delta^{13}C_0$ response to obliquity forcing was explored using a second isotopic mass balance model (setup THM, THOt, and THCpr in section 2; Figure 6). The experiments suggest that a combination of the ~100 kyr residence time and quasi-stable behavior of a fraction of the exogenic carbon inventory will produce a major Myr-scale cyclicity that is compatible with the pattern observed in Bch-1 (Figures 4 and 6) and, on a Myr scale, provides a better fit to the data than eccentricity-modulated, precession-driven models [*Laurin et al*., 2014] (Figures S4.8–S4.11 in the supporting information). Notably, the spectrum of the simulated $\delta^{13}C_0$ indicates a relative dominance of the ~1 and ~2.5 Myr cycles (Figure 6f) that is consistent with the Bch-1 data (Figure 3a). For methane ($\varepsilon = -60‰$) and bulk organic matter ($\varepsilon = -26‰$), without feedbacks, the maximum rates of reservoir buildup required in this model are 4 and 9 Pg of carbon per kyr (PgC/kyr), respectively, which is 6–13% of the background organic burial. The model reservoirs reach a maximum size of 3500 PgC (methane carbon) and 6400 PgC (bulk organic carbon), with 28–61 PgC/kyr outgassing rates upon destabilization. The drop in the net carbon burial accompanying reservoir decay is relatively high (Figure 6), but it does not require a change in organic productivity; the excess input flux responsible for the decline in net burial is sourced from the existing quasi-stable reservoir. Similar results can be obtained with the opposite phasing of the reservoir buildup/decay relative to axial obliquity. If the reservoir buildup is aligned with increasing obliquity, however, the asymmetry of buildup rates versus outgassing rates changes. To successfully reproduce the observed $\delta^{13}C$ signature, the model requires buildup rates in the order of 30 PgC/kyr (methane carbon; Figure S4.7 in the supporting information) and 60 PgC/kyr (bulk organic carbon; Figure S4.6 in the supporting information). Somewhat lower fluxes would be sufficient for a reservoir dominated by marine organic matter with $\varepsilon < -26‰$.

Marine carbonate reservoirs (setup THCpr) require buildup rates of >160 PgC/kyr (>58% of the net inorganic carbon burial flux), a reservoir size of over 100,000 PgC, and dissolution rates of >1200 PgC/kyr to replicate the observed $\delta^{13}C$ pattern (Figure S4.3 in the supporting information). Even when supported by weathering and ocean chemistry feedbacks (see Text S2 in the supporting information), the THCpr scenario would be equivalent to (or more likely exceed) cycles of a complete collapse and subsequent recovery of neritic carbonate production [cf. *Weissert et al*., 1998; *Donnadieu et al*., 2011]. These changes would have to involve major dissolution episodes and occur systematically, in a ~40 kyr rhythm. It should be noted that all of the above models tend to overestimate the rates and amounts of carbon required to replicate $\delta^{13}C_{org}$ and $\delta^{13}C_{carb}$ excursions, because they do not consider the effect of evolving pCO_2 on carbon-isotope fractionation. Organic carbon accumulation, methane storage, and carbonate dissolution—the processes that drive $\delta^{13}C_0$ toward ^{13}C-enriched values—result in a drawdown of atmospheric CO_2, which in turn affects the photosynthetic fractionation of carbon isotopes [e.g., *Freeman and Hayes*, 1992; *Pagani et al*., 1999; *Kump and Arthur*, 1999]. Changes in $\delta^{13}C_{org}$ observed in Bch-1 and other records are therefore mixed products of $\delta^{13}C_0$ variations and other factors including the fractionation effects of pCO_2 changes. When scaled relative to a $\delta^{13}C_0$ change per mole of carbon, the effect on pCO_2 is highest for carbonate. Theoretically, the accumulation and dissolution of carbonate could therefore impart a major role via changes in pCO_2 rather than via changes in $\delta^{13}C_0$. This effect should, however, be documented by changing differences between $\delta^{13}C_{org}$ and $\delta^{13}C_{carb}$ [e.g., *Kump and Arthur*, 1999; *Louis-Schmid et al*., 2007; *Jarvis et al*., 2011]. The available data do not support this possibility. In the interval covered by Bch-1 data, the differences between ~1 Myr magnitudes in $\delta^{13}C_{org}$ and $\delta^{13}C_{carb}$ do not exceed 0.3‰. In spite of localized decoupling of $\delta^{13}C_{org}$ from $\delta^{13}C_{carb}$ (e.g., the Late Turonian Hitch Wood CIE), most CIEs are equally prominent in $\delta^{13}C_{carb}$ as they are in $\delta^{13}C_{org}$ suggesting that fractionation

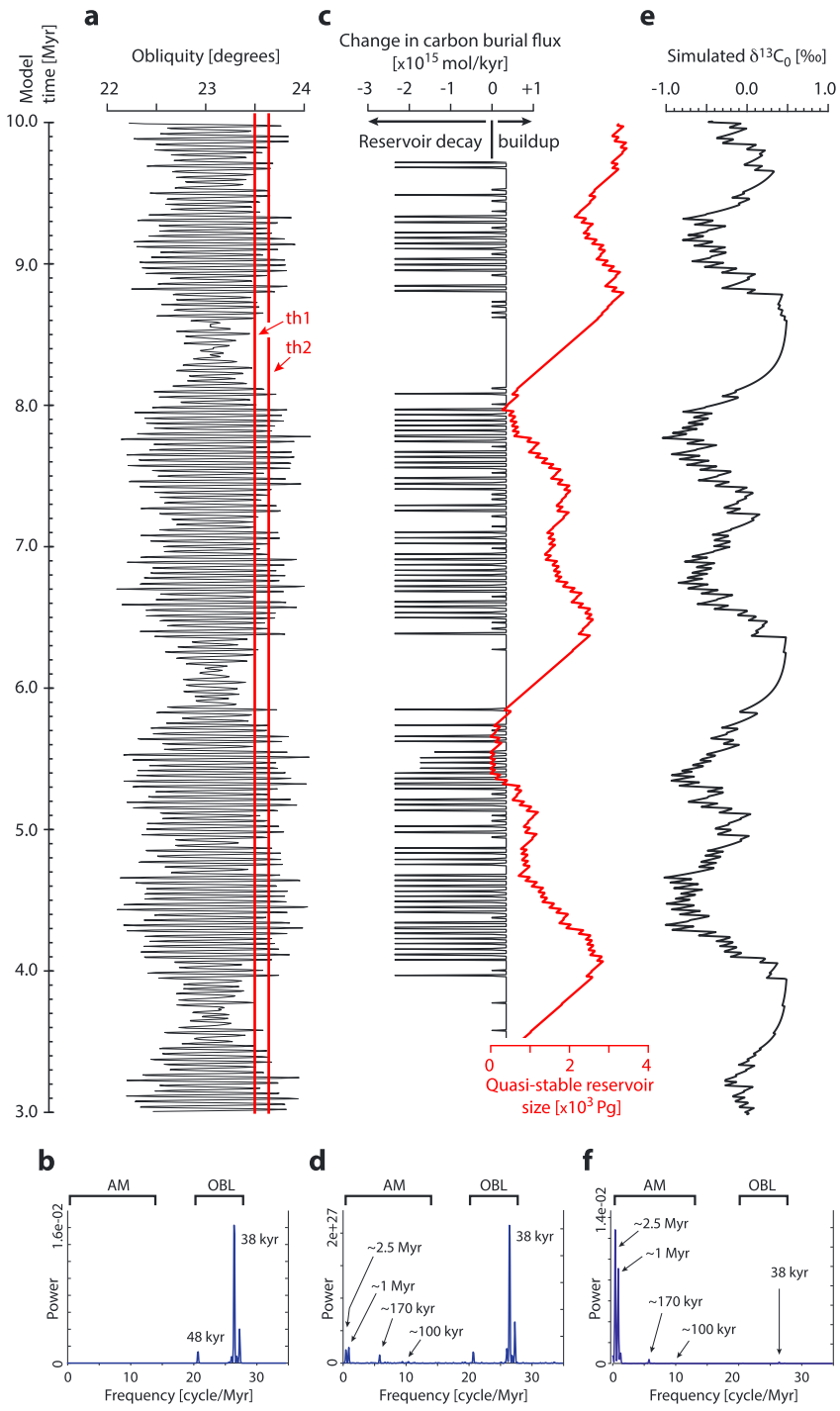

Figure 6. Input and output parameters of the quasi-stable reservoir model, which provides the best fit to the data by simulating methane-carbon burial and release in response to obliquity variations (setup THM-OBL-La04; see section 2 and Table S2.2 in the supporting information). The mean residence time of carbon is 121 kyr. (a) Input obliquity forcing. The reservoir is assumed to act as a carbon sink for obliquity values below threshold th1 and is reconfigured to become a net carbon source when obliquity increases above th2. Note that a similar pattern in $\delta^{13}C_0$ can be obtained with the opposite phasing, i.e., reservoir buildup at high obliquity (Figure S4.7 in the supporting information). (b) Periodogram of the input obliquity (OBL) signal. (c) Rates of the reservoir buildup and decay (black) and the size of the reservoir (red) simulated as a simple threshold response to obliquity forcing. (d) Periodogram of the simulated carbon burial flux. Note that a small amount of variance is transferred to AM wavelengths, but the signal is still dominated by the primary obliquity frequencies. (e) Simulated $\delta^{13}C_0$. (f) Periodogram of the output $\delta^{13}C_0$. Note the prominence of AM wavelengths, namely, the ~1 Myr term. See Figures S4.2–S4.12 in the supporting information for alternative models.

effects were of secondary importance in driving these excursions. In summary, carbonate storage/dissolution alone appears to be an unlikely source of the ~1 Myr scale cycles of $\delta^{13}C$ observed in the study interval.

3.4. Axial Obliquity Control on the Carbon Budget

Most Milankovitch-like rhythms identified in the Cretaceous have been attributed to the cycle of axial precession (whose climatic effect is modulated by eccentricity) or a combination of precession/eccentricity and minor obliquity (Table S3 in the supporting information). This link can be understood in the context of the dominant control that the precessional/eccentricity cycle imparts on the seasonal insolation intensity [*Berger et al*., 1993] and the lengths of seasons [*Huybers and Denton*, 2008]. Obliquity, in contrast, is of secondary importance in most seasonal insolation series. Its climatic effect increases toward high latitudes, but only winter insolation near the polar circle, integrated summer insolation at high latitudes, or annual insolation (at all latitudes) exhibit orbital-scale changes that are dominated by obliquity (see discussion in *Huybers* [2006]). The changes in annual insolation are very small and their climatic effect is questionable, but changing winter insolation near the polar circle can affect high-latitude biomass production by controlling the extent of polar night regions. Integrated summer insolation has been proposed as the principal control on incipient ice sheets [*Huybers*, 2006] and should therefore affect the extent of permafrost—an important methane-carbon pool (see below). Obliquity is also the principal control on astronomical-scale changes in the meridional insolation gradients (namely, between middle and high latitudes), which affect poleward atmospheric moisture transport [*Raymo and Nisancioglu*, 2003]. The scarcity of obliquity-dominated sedimentary rhythms at low latitudes in the Late Cretaceous (except for parts of OAE II; [*Meyers et al*., 2012b]) supports the theoretical expectation that the sources of strong obliquity AM signal in $\delta^{13}C$ were located in high- or middle-latitude regions. Available data point to three potential sources of the isotopic signature:

1. Obliquity-paced organic matter accumulation is documented near the culmination of OAE II [*Meyers et al*., 2012b]. Shallow-buried, organic carbon-rich deposits occurring in the marginal zones of marine euxinic settings might have therefore acted as quasi-stable carbon reservoirs in pace with the hypothesized ~1 Myr rhythm (Figure 1). This concept is consistent with the importance of local and regional processes in controlling euxinic conditions during OAE II [e.g., *Trabucho Alexandre et al*., 2010; *Owens et al*., 2013]. If the documented increase in obliquity variance (and decrease in eccentricity variance) toward the peak OAE II reflects an inherent AM of the astronomical signal, then the reservoir expansion would have to be tied to increasing obliquity, i.e., the "reverse" model setup would apply (Figure S4.6 in the supporting information). Alternatively, the change in obliquity variance could be a signature of increased sensitivity of the Atlantic depositional sites to high-latitude processes, possibly via accelerated intermediate/deep water production augmented by transient cooling [*Meyers et al*., 2012b]. This scenario should respond to weak summer insolation at high latitudes, which is supported by low obliquity, thus favoring a low-obliquity phasing of the reservoir buildup (Figure S4.2 in the supporting information). In any instance, the nonlinear response of the carbon cycle to obliquity forcing was exaggerated by nutrient delivery from hydrothermal sources during the OAE II [*Snow et al*., 2005; *Turgeon and Creaser*, 2008; *Flögel et al*., 2011a; *Du Vivier et al*., 2014].
2. Organic matter storage in midlatitude lakes and soils provides another possibility. A powerful potential can be expected in arid and semiarid regions of Asia that underwent major climate shifts during the Late Cretaceous [*Wang et al*., 2013] and have been shown to be sensitive to obliquity forcing under relatively warm climates [e.g., *Bosboom et al*., 2014]. This link is supported by a notably strong ~1.2 Myr signature in magnetic susceptibility data from the inland Songliao Basin of NE China (~45°N) [*Wu et al*., 2013], which likely reflects changes in the local or regional hydrology. Other climate-sensitive carbon reservoirs were nested in the midlatitudes of South America [*Basilici et al*., 2009] and Africa [*Floegel and Wagner*, 2006], but their response to astronomical forcing is either uncertain (South America) or dominated by precession (Africa) [*Beckmann et al*., 2005; *Floegel and Wagner*, 2006].
3. Finally, methane carbon would be the most efficient agent, due to its contrasting $\delta^{13}C$ composition and high production rates at high latitudes of the greenhouse world [*Beerling et al*., 2011]. Because climate modeling suggests the possibility of interannual ice accumulation [*Flögel et al*., 2011b] and permafrost storage of up to 3700 PgC at pCO_2 levels above 750 ppmv [*DeConto et al*., 2012], the role of astronomically paced interplay of wetlands and cryosphere fluctuations in the carbon budget should be considered for the Late Cretaceous greenhouse. The rate of methane fixation needed to develop realistic $\delta^{13}C_0$

patterns is 6 Tg/yr (Tg = 10^{12} g) for model scenarios in which the reservoir buildup is supported by low obliquity (Figure 6 and Figures S4.4–S4.5 in the supporting information). This rate is equivalent to ~3% of the methane production rate estimated for the southern middle to high latitudes of the Late Cretaceous [*Beerling et al*., 2011]. The opposite phasing, i.e., reservoir expansion with increasing obliquity (Figure S4.7 in the supporting information), requires higher buildup rates (~38 Tg of methane per year). Such a phasing is, however, incompatible with permafrost storage [cf. *DeConto et al*., 2012].

Additional data will be needed to determine whether Myr-scale maxima in $\delta^{13}C$ trace the nodes or highs in the obliquity AM. The different types of carbon reservoirs might have interfered both positively and negatively in their effect on $\delta^{13}C_0$ (depending on the preferred obliquity phasing), and the relative importance of individual reservoirs likely varied in the course of the Late Cretaceous. The persistent signature of ~1 Myr AM of axial obliquity, however, suggests that—on the Myr time scale—the net effect of this interference was stable throughout the Late Cenomanian-Campanian interval. Colder intervals of the Cretaceous and Cenozoic lack the ~1 Myr cyclicity in carbon-isotope records [cf. *Cramer et al*., 2003; *Pälike et al*., 2006; *Giorgioni et al*., 2012], suggesting that this type of reservoir behavior might have been related to the distinct conditions of the peak greenhouse warmth. A possible link to accelerated continental weathering, enhanced nutrient fluxes [cf. *Föllmi*, 1996; *Handoh and Lenton*, 2003; *Sprovieri et al*., 2013; *von Strandmann et al*., 2013], and high biomass production at high latitudes [cf. *Beerling et al*., 2011] should be further explored.

4. Conclusions

The Late Cretaceous carbon budget was controlled on a ~1 Myr scale by amplitude modulation of axial obliquity. The nonlinear transfer of variance from the primary obliquity signal to AM periods is difficult to explain solely by the residence time of carbon. We offer a nonlinear mechanism involving recycling of carbon on astronomical time scales by episodic formation and decay of reservoirs of organic matter and/or methane (e.g., terrestrial peat, soil and lakes, permafrost, and marginal parts of marine euxinic settings). The obliquity signature suggests that these reservoirs responded to high-latitude insolation or middle- to high-latitude insolation gradients. The quasi-stable character of this type of reservoirs dictates their low preservation potential. They are probably underrepresented in the geological record, but their role in controlling the Myr-scale variability in the greenhouse climate might have been prominent. In the colder Cenozoic world, the ~1 Myr rhythm of these carbon transfers became clearly established in glacial cyclicity but faded from the $\delta^{13}C$ record [*Pälike et al*., 2006], suggesting that the Late Cretaceous reservoirs had vanished or become less efficient (e.g., due to reduced biomass production at high latitudes and/or decelerated continental weathering and nutrient fluxes). The principle of orbitally paced carbon storage in quasi-stable reservoirs might be universal. It would help to explain multi-Myr-scale cyclicity in the Cenozoic $\delta^{13}C$ that has been proposed to follow a secular modulation of orbital eccentricity [*Boulila et al*., 2012] and may be linked to the origin of major Paleocene-Eocene hyperthermals [*DeConto et al*., 2012; *Boulila et al*., 2012; *Komar et al*., 2013]. A closer characterization of the locations and functioning of these reservoirs will be important for unraveling the carbon cycle dynamics in both greenhouse and icehouse worlds.

Acknowledgments

Data used in this paper may be obtained from Jiří Laurin (e-mail: laurin@ig.cas.cz). Supporting information text, figures, and tables include details on carbon-isotope correlation, age models, and isotopic mass balance simulations. This research was supported by the Ministry of Education (grant LH12041 to J.L.) and the Czech Science Foundation (grant P210/10/1991 to D.U.). D.U. and J.L. acknowledge support by research program RVO67985530 of the Academy of Sciences of the Czech Republic. I.J. was funded by UK Natural Environment Research Council (NERC) grant NE/H020756/1. S.R.M. and B.B.S. acknowledge support from NSF EAR-0959108. We are grateful for the constructive comments from the reviewers Graham Weedon and Mario Sprovieri that helped to improve the manuscript.

References

Anderson, L. G., D. Dyrssen, and J. Skei (1987), Formation of chemogenic calcite in super-anoxic seawater—Framvaren, southern Norway, *Mar. Chem.*, *20*, 361–376, doi:10.1016/0304-4203(87)90068-5.

Arthur, M. A., W. E. Dean, and L. M. Pratt (1988), Geochemical and climatic effects of increased marine organic carbon burial at the Cenomanian/Turonian boundary, *Nature*, *335*, 714–717, doi:10.1038/335714a0.

Basilici, G., P. F. F. Dal Bó, and F. S. B. Ladeira (2009), Climate-induced sediment-palaeosol cycles in a Late Cretaceous dry aeolian sand sheet: Marília Formation (North-West Bauru Basin, Brazil), *Sedimentology*, *56*, 1876–1904, doi:10.1111/j.1365-3091.2009.01061.x.

Batenburg, S. J., et al. (2012), Cyclostratigraphy and astronomical tuning of the Late Maastrichtian at Zumaia (Basque country, Northern Spain), *Earth Planet. Sci. Lett.*, *359–360*, 264–278, doi:10.1016/j.epsl.2012.09.054.

Beaufort, L. (1994), Climatic importance of the modulation of the 100 kyr cycle inferred from 16 m.y. long Miocene records, *Paleoceanography*, *9*, 821–834, doi:10.1029/94PA02115.

Beckmann, B., S. Flögel, P. Hofmann, M. Schulz, and T. Wagner (2005), Orbital forcing of Cretaceous river discharge in tropical Africa and ocean response, *Nature*, *437*, 241–244, doi:10.1038/nature03976.

Beerling, D. J., A. Fox, D. S. Stevenson, and P. J. Valdes (2011), Enhanced chemistry-climate feedbacks in past greenhouse worlds, *Proc. Natl. Acad. Sci. U.S.A.*, *108*, 9770–9775, doi:10.1073/pnas.1102409108.

Berger, A., M.-F. Loutre, and C. Tricot (1993), Insolation and Earth's orbital periods, *J. Geophys. Res.*, *98*(D6), 10,341–10,362, doi:10.1029/93JD00222.

Berner, R. A. (1987), Models for carbon and sulfur cycles and atmospheric oxygen: Application to Paleozoic history, *Am. J. Sci.*, *287*, 177–196, doi:10.2475/ajs.287.3.177.

Berner, R. A. (2006), GEOCARBSULF: A combined model for Phanerozoic atmospheric O_2 and CO_2, *Geochim. Cosmochim. Acta*, *70*, 5653–5664, doi:10.1016/j.gca.2005.11.032.

Berner, R. A., and D. E. Canfield (1989), A new model of atmospheric oxygen over Phanerozoic time, *Am. J. Sci.*, *289*, 333–361, doi:10.2475/ajs.289.4.333.

Blackman, R. B., and J. W. Tukey (1958), *The Measurement of Power Spectra From the Point of View of Communication Engineering*, Dover, New York.

Bosboom, R. E., H. A. Abels, C. Hoorn, B. C. J. van den Berg, Z. Guo, and G. Dupont-Nivet (2014), Aridification in continental Asia after the Middle Eocene Climatic Optimum (MECO), *Earth Planet. Sci. Lett.*, *389*, 34–42, doi:10.1016/j.epsl.2013.12.014.

Boulila, S., B. Galbrun, K. G. Miller, S. F. Pekar, J. V. Browning, J. Laskar, and J. D. Wright (2011), On the origin of Cenozoic and Mesozoic "third-order" eustatic sequences, *Earth Sci. Rev.*, *109*, 94–112, doi:10.1016/j.earscirev.2011.09.003.

Boulila, S., B. Galbrun, J. Laskar, and H. Pälike (2012), A ~9 myr cycle in Cenozoic $\delta^{13}C$ record and long-term orbital eccentricity modulation: Is there a link?, *Earth Planet. Sci. Lett.*, *317*, 273–281.

Clarke, L. J., and H. C. Jenkyns (1999), New oxygen isotope evidence for long-term Cretaceous climatic change in the Southern Hemisphere, *Geology*, *27*, 699–702, doi:10.1130/0091-7613(1999)027<0699:NOIEFL>2.3.CO;2.

Cramer, B. S., J. D. Wright, D. V. Kent, and M. P. Aubry (2003), Orbital climate forcing of $\delta^{13}C$ excursions in the late Paleocene–early Eocene (chrons C24n–C25n), *Paleoceanography*, *18*(4), 1097, doi:10.1029/2003PA000909.

Cramer, B. S., J. R. Toggweiler, J. D. Wright, M. E. Katz, and K. G. Miller (2009), Ocean overturning since the Late Cretaceous: Inferences from a new benthic foraminiferal isotope compilation, *Paleoceanography*, *24*, PA4216, doi:10.1029/2008PA001683.

DeConto, R. M., S. Galeotti, M. Pagani, D. Tracy, K. Schaefer, T. Zhang, D. Pollard, and D. J. Beerling (2012), Past extreme warming events linked to massive carbon release from thawing permafrost, *Nature*, *484*, 87–92, doi:10.1038/nature10929.

Dickens, G. R. (2003), Rethinking the global carbon cycle with a large, dynamic and microbially mediated gas hydrate capacitor, *Earth Planet. Sci. Lett.*, *213*, 169–183, doi:10.1016/S0012-821X(03)00325-X.

Donnadieu, Y., G. Dromart, Y. Goddéris, E. Pucéat, B. Brigaud, G. Dera, C. Dumas, and N. Olivier (2011), A mechanism for brief glacial episodes in the Mesozoic greenhouse, *Paleoceanography*, *26*, PA3212, doi:10.1029/2010PA002100.

Du Vivier, A. D. C., D. Selby, B. B. Sageman, I. Jarvis, D. R. Gröcke, and S. Voigt (2014), Marine $^{187}Os/^{188}Os$ isotope stratigraphy reveals the interaction of volcanism and ocean circulation during Oceanic Anoxic Event 2, *Earth Planet. Sci. Lett.*, *389*, 23–33, doi:10.1016/j.epsl.2013.12.024.

Floegel, S., and T. Wagner (2006), Insolation-control on the Late Cretaceous hydrological cycle and tropical African climate—Global climate modelling linked to marine climate records, *Palaeogeogr. Palaeoclimatol. Palaeoecol.*, *235*, 288–304, doi:10.1016/j.palaeo.2005.09.034.

Flögel, S., K. Wallmann, C. J. Poulsen, J. Zhou, A. Oschlies, S. Voigt, and W. Kuhnt (2011a), Simulating the biogeochemical effects of volcanic CO_2 degassing on the oxygen-state of the deep ocean during the Cenomanian/Turonian Anoxic Event (OAE2), *Earth Planet. Sci. Lett.*, *305*, 371–384, doi:10.1016/j.epsl.2011.03.018.

Flögel, S., K. Wallmann, and W. Kuhnt (2011b), Cool episodes in the Cretaceous—Exploring the effects of physical forcings on Antarctic snow accumulation, *Earth Planet. Sci. Lett.*, *307*, 279–288, doi:10.1016/j.epsl.2011.04.024.

Föllmi, K. B. (1996), The phosphorus cycle, phosphogenesis and marine phosphate-rich deposits, *Earth Sci. Rev.*, *40*, 55–124, doi:10.1016/0012-8252(95)00049-6.

Forster, A., S. Schouten, M. Baas, and J. S. Sinninghe Damsté (2007), Mid-Cretaceous (Albian-Santonian) sea surface temperature record of the tropical Atlantic Ocean, *Geology*, *35*, 919–922, doi:10.1130/G23874A.1.

Freeman, K. H., and J. M. Hayes (1992), Fractionation of carbon isotopes by phytoplankton and estimates of ancient CO_2 levels, *Global Biogeochem. Cycles*, *6*, 185–198, doi:10.1029/92GB00190.

Friedrich, O., R. D. Norris, and J. Erbacher (2012), Evolution of middle to Late Cretaceous oceans—A 55 m.y. record of Earth's temperature and carbon cycle, *Geology*, *40*, 107–110, doi:10.1130/G32701.1.

Gilman, D. L., F. J. Fuglister, and J. M. Mitchell Jr. (1963), On the power spectrum of 'red noise', *J. Atmos. Sci.*, *20*, 182–184.

Giorgioni, M. (2012), Long- and short-term changes in Tethyan oceanography and in global carbon cycling during Albian-Cenomanian time, PhD thesis, ETH Zurich.

Giorgioni, M., H. Weissert, S. M. Bernasconi, P. A. Hochuli, R. Coccioni, and C. E. Keller (2012), Orbital control on carbon cycle and oceanography in the mid-Cretaceous greenhouse, *Paleoceanography*, *27*, PA1204, doi:10.1029/2011PA002163.

Handoh, I. C., and T. M. Lenton (2003), Periodic mid-Cretaceous oceanic anoxic events linked by oscillations of the phosphorus and oxygen biogeochemical cycles, *Global Biogeochem. Cycles*, *17*(4), 1092, doi:10.1029/2003GB002039.

Hayes, J. M., H. Strauss, and A. J. Kaufman (1999), The abundance of ^{13}C in marine organic matter and isotopic fractionation in the global biogeochemical cycle of carbon during the past 800 Ma, *Chem. Geol.*, *161*, 103–125, doi:10.1016/S0009-2541(99)00083-2.

Herbert, T. D. (1997), A long marine history of carbon cycle modulation by orbital-climatic changes, *Proc. Natl. Acad. Sci. U.S.A.*, *94*, 8362–8369.

Herbert, T. D., J. Gee, and S. DiDonna (1999), Precessional cycles in Upper Cretaceous pelagic sediments of the South Atlantic: Long-term patterns from high-frequency climate variations, in *Evolution of the Cretaceous Ocean-Climate System*, edited by E. Barrera and C. C. Johnson, *Geol. Soc. Am. Spec. Pap.*, *332*, 105–120.

Huybers, P. J. (2006), Early Pleistocene glacial cycles and the integrated summer insolation forcing, *Science*, *313*, 508–511, doi:10.1126/science.1125249.

Huybers, P. J., and G. Denton (2008), Antarctic temperature at orbital timescales controlled by local summer duration, *Nat. Geosci.*, *1*, 787–792, doi:10.1038/ngeo311.

Imbrie, J., et al. (1993), On the structure and origin of major glaciation cycles: 2. The 100,000-year cycle, *Paleoceanography*, *8*, 699–735, doi:10.1029/93PA02751.

Jarvis, I., A. S. Gale, H. C. Jenkyns, and M. A. Pearce (2006), Secular variation in Late Cretaceous carbon isotopes: A new $\delta^{13}C$ carbonate reference curve for the Cenomanian-Campanian (99.6–70.6 Ma), *Geol. Mag.*, *143*, 561–608, doi:10.1017/S0016756806002421.

Jarvis, I., J. S. Lignum, D. R. Gröcke, H. C. Jenkyns, and M. A. Pearce (2011), Black shale deposition, atmospheric CO_2 drawdown, and cooling during the Cenomanian-Turonian Oceanic Anoxic Event, *Paleoceanography*, *26*, PA3201, doi:10.1029/2010PA002081.

Joo, Y. J., and B. B. Sageman (2014), Cenomanian to Campanian carbon isotope chemostratigraphy from the Western Interior Basin, U.S.A, *J. Sediment. Res.*, *84*, 529–542, doi:10.2110/jsr.2014.38.

Komar, N., R. E. Zeebe, and G. R. Dickens (2013), Understanding long-term carbon cycle trends: The late Paleocene through the early Eocene, *Paleoceanography*, *28*, 650–662, doi:10.1002/palo.20060.

Kump, L. R. (1991), Interpreting carbon-isotope excursions: Strangelove oceans, *Geology*, *19*, 299–302, doi:10.1130/0091-7613(1991)019<0299:ICIESO>2.3.CO;2.

Kump, L. R., and M. A. Arthur (1999), Interpreting carbon–isotope excursions: Carbonate and organic matter, *Chem. Geol.*, *161*, 181–198, doi:10.1016/S0009-2541(99)00086-8.
Kurtz, A. C., L. R. Kump, M. A. Arthur, J. C. Zachos, and A. Paytan (2003), Early Cenozoic decoupling of the global carbon and sulfur cycles, *Paleoceanography*, *18*(4), 1090, doi:10.1029/2003PA000908.
Lanci, L., G. Muttoni, and E. Erba (2010), Astronomical tuning of the Cenomanian Scaglia Bianca Formation at Furlo, Italy, *Earth Planet. Sci. Lett.*, *292*, 231–237, doi:10.1016/j.epsl.2010.01.041.
Laskar, J., F. Joutel, and F. Boudin (1993), Orbital, precessional, and insolation quantities for the Earth from −20 Myr to +10 Myr, *Astron. Astrophys.*, *270*, 522–533.
Laskar, J., P. Robutel, F. Joutel, M. Gastineau, A. C. M. Correia, and B. Levrard (2004), A long-term numerical solution for the insolation quantities of the Earth, *Astron. Astrophys.*, *428*, 261–285, doi:10.1051/0004-6361:20041335.
Laskar, J., A. Fienga, M. Gastineau, and H. Manche (2011), La2010: A new orbital solution for the long-term motion of the Earth, *Astron. Astrophys.*, *532*, A89, doi:10.1051/0004-6361/201116836.
Laurin, J., S. R. Meyers, B. B. Sageman, and D. Waltham (2005), Phase-lagged amplitude modulation of hemipelagic cycles: A potential tool for recognition and analysis of sea level change, *Geology*, *33*, 569–572, doi:10.1130/G21350.1.
Laurin, J., S. Čech, D. Uličný, Z. Štaffen, and M. Svobodová (2014), Astrochronology of the Late Turonian: Implications for the behavior of the carbon cycle at the demise of peak greenhouse, *Earth Planet. Sci. Lett.*, *394*, 254–269, doi:10.1016/j.epsl.2014.03.023.
Locklair, R., B. Sageman, and A. Lerman (2011), Marine carbon burial flux and the carbon isotope record of Late Cretaceous (Coniacian-Santonian) Oceanic Anoxic Event III, *Sediment. Geol.*, *235*, 38–49, doi:10.1016/j.sedgeo.2010.06.026.
Louis-Schmid, B., P. Rais, P. Schaeffer, S. M. Bernasconi, and H. Weissert (2007), Plate tectonic trigger of changes in pCO_2 and climate in the Oxfordian (Late Jurassic): Carbon isotope and modeling evidence, *Earth Planet. Sci. Lett.*, *258*, 44–60, doi:10.1016/j.epsl.2007.03.014.
Ma, C., S. R. Meyers, B. B. Sageman, B. S. Singer, and B. R. Jicha (2014), Testing the astronomical time scale for oceanic anoxic event 2, and its extension into Cenomanian strata of the Western Interior Basin (USA), *Geol. Soc. Am. Bul.*, *126*, 974–989, doi:10.1130/B30922.1.
Ma, W., J. Tian, Q. Li, and P. Wang (2011), Simulation of long eccentricity (400-kyr) cycle in ocean carbon reservoir during Miocene Climate Optimum: Weathering and nutrient response to orbital change, *Geophys. Res. Lett.*, *38*, L10701, doi:10.1029/2011GL047680.
MacLeod, K. G., B. T. Huber, Á. J. Berrocoso, and I. Wendler (2013), A stable and hot Turonian without glacial $\delta^{18}O$ excursions is indicated by exquisitely preserved Tanzanian foraminifera, *Geology*, *41*, 1083–1086, doi:10.1130/G34510.1.
Mann, M. E., and J. M. Lees (1996), Robust estimation of background noise and signal detection in climatic time series, *Clim. Change*, *33*, 409–445, doi:10.1007/BF00142586.
Marin-Spiotta, E., N. T. Chaopricha, A. F. Plante, A. F. Diefendorf, C. W. Mueller, A. S. Grandy, and J. A. Mason (2014), Long-term stabilization of deep soil carbon by fire and burial during early Holocene climate change, *Nat. Geosci.*, *7*, 428–432, doi:10.1038/ngeo2169.
Meister, P., J. A. McKenzie, C. Vasconcelos, S. Bernasconi, M. Frank, M. Gutjahr, and D. P. Schrag (2007), Dolomite formation in the dynamic deep biosphere, results from the Peru Margin, OPD Leg 201, *Sedimentology*, *54*, 1007–1032, doi:10.1111/j.1365-3091.2007.00870.x.
Meyers, P. A. (2014), Why are the $\delta^{13}C_{org}$ values in Phanerozoic black shales more negative than in modern marine organic matter?, *Geochem. Geophys. Geosyst.*, *15*, 3085–3106, doi:10.1002/2014GC005305.
Meyers, S. R. (2012), Seeing red in cyclic stratigraphy: Spectral noise estimation for astrochronology, *Paleoceanography*, *27*, PA3228, doi:10.1029/2012PA002307.
Meyers, S. R. (2014), Astrochron: An R package for astrochronology (Version 0.3.1). [Available at http://www.geology.wisc.edu/~smeyers.]
Meyers, S. R., B. B. Sageman, and L. A. Hinnov (2001), Integrated quantitative stratigraphy of the Cenomanian-Turonian bridge creek limestone member using evolutive harmonic analysis and stratigraphic modeling, *J. Sediment. Res.*, *71*, 627–643.
Meyers, S. R., S. E. Siewert, B. S. Singer, B. B. Sageman, D. J. Condon, J. D. Obradovich, B. R. Jicha, and D. A. Sawyer (2012a), Intercalibration of radioisotopic and astrochronologic time scales for the Cenomanian-Turonian boundary interval, Western Interior Basin, USA, *Geology*, *40*, 7–10, doi:10.1130/G32261.1.
Meyers, S. R., B. B. Sageman, and M. A. Arthur (2012b), Obliquity forcing of organic matter accumulation during Oceanic Anoxic Event 2, *Paleoceanography*, *27*, PA3212, doi:10.1029/2012PA002286.
Mitchell, R. N., D. M. Bice, A. Montanari, L. C. Cleaveland, K. T. Christianson, R. Coccioni, and L. A. Hinnov (2008), Oceanic anoxic cycles? Orbital prelude to the Bonarelli Level (OAE 2), *Earth Planet. Sci. Lett.*, *26*, 1–16, doi:10.1016/j.epsl.2007.11.026.
Mudelsee, M. (2010), *Climate Times Series Analysis: Classical Statistical and Bootstrap Methods*, Springer, Dordrecht, Netherlands.
Naehr, T. H., P. Eichhubl, V. J. Orphan, M. Hovland, C. K. Paull, W. Ussler III, T. D. Lorenson, and H. G. Greene (2007), Authigenic carbonate formation at hydrocarbon seeps in continental margin sediments: A comparative study, *Deep Sea Res., Part II*, *54*, 1268–1291, doi:10.1016/j.dsr2.2007.04.010.
Ogg, J. G., and L. A. Hinnov (2012), Cretaceous, in *The Geologic Time Scale 2012*, edited by F. M. Gradstein et al., pp. 793–853, Elsevier, Amsterdam.
O'Reilly, S. S., K. Hryniewicz, C. T. S. Little, X. Monteys, M. T. Szpak, B. T. Murphy, S. F. Jordan, C. C. R. Allen, and B. P. Kelleher (2014), Shallow water methane-derived authigenic carbonate mounds at the Codling Fault Zone, western Irish Sea, *Mar. Geol.*, *357*, 139–150, doi:10.1016/j.margeo.2014.08.007.
Owens, J. D., B. C. Gill, H. C. Jenkyns, S. M. Bates, S. Severmann, M. M. M. Kuypers, R. G. Woodfine, and T. W. Lyons (2013), Sulfur isotopes track the global extent and dynamics of euxinia during Cretaceous Oceanic Anoxic Event 2, *Proc. Natl. Acad. Sci. U.S.A.*, *110*, 18,407–18,412, doi:10.1073/pnas.1305304110.
Pagani, M., M. A. Arthur, and K. H. Freeman (1999), Miocene evolution of atmospheric carbon dioxide, *Paleoceanography*, *14*, 273–292, doi:10.1029/1999PA900006.
Paillard, D., and Y. Donnadieu (2014), A 100 Myr history of the carbon cycle based on the 400 kyr cycle in marine $\delta^{13}C$ benthic records, *Paleoceanography*, *29*, 1249–1255, doi:10.1002/2014PA002693.
Paillard, D., L. Labeyrie, and P. Yiou (1996), Macintosh program performs time-series analysis, *Eos Trans. AGU*, *77*, 379.
Pälike, H., R. D. Norris, J. O. Herrle, P. A. Wilson, H. K. Coxall, C. H. Lear, N. J. Shackleton, A. K. Tripati, and B. S. Wade (2006), The heartbeat of the Oligocene climate system, *Science*, *314*, 1894–1898, doi:10.1126/science.1133822.
Percival, D. P., and A. T. Walden (1998), *Spectral Analysis for Physical Applications*, Cambridge Univ. Press, Cambridge.
Pucéat, E., C. Lecuyer, S. M. F. Sheppard, G. Dromart, S. Reboulet, and P. Grandjean (2003), Thermal evolution of Cretaceous Tethyan marine waters inferred from oxygen isotope composition of fish tooth enamels, *Paleoceanography*, *18*(2), 1029, doi:10.1029/2002PA000823.
Raymo, M. E., and K. Nisancioglu (2003), The 41 kyr world: Milankovitch's other unsolved mystery, *Paleoceanography*, *18*(1), 1011, doi:10.1029/2002PA000791.
Reimers, C. E., K. C. Ruttenberg, D. E. Canfield, M. B. Christiansen, and J. B. Martin (1996), Porewater pH and authigenic phases formed in the uppermost sediments of the Santa Barbara Basin, *Geochim. Cosmochim. Acta*, *60*, 4037–4057, doi:10.1016/S0016-7037(96)00231-1.

Roberts, H. H., and P. Aharon (1994), Hydrocarbon-derived carbonate buildups of the northern Gulf of Mexico continental slope: A review of submersible investigations, *Geo-Mar. Lett.*, *14*, 135–148, doi:10.1007/BF01203725.

Sageman, B. B., S. R. Meyers, and M. A. Arthur (2006), Orbital time scale and new C-isotope record for Cenomanian-Turonian boundary stratotype, *Geology*, *34*, 125–128, doi:10.1130/G22074.1.

Sageman, B. B., B. S. Singer, S. R. Meyers, S. E. Seiwert, I. Walaszczyk, D. J. Condon, B. R. Jicha, J. D. Obradovich, and D. A. Sawyer (2014), Integrating $^{40}Ar/^{39}Ar$, U-Pb, and astronomical clocks in the Cretaceous Niobrara Formation, Western Interior Basin, USA, *Geol. Soc. Am. Bull.*, *126*, 956–973, doi:10.1130/B30929.1.

Schrag, D. P., J. A. Higgins, F. A. Macdonald, and D. T. Johnson (2013), Authigenic carbonate and the history of the global carbon cycle, *Science*, *339*, 540–543, doi:10.1126/science.1229578.

Short, D. A., J. G. Mengel, T. J. Crowley, W. T. Hyde, and G. R. North (1991), Filtering of Milankovitch cycles by Earth's geography, *Quat. Res.*, *35*, 157–173, doi:10.1016/0033-5894(91)90064-C.

Snow, L. J., R. A. Duncan, and T. J. Bralower (2005), Trace element abundances in the Rock Canyon Anticline, Pueblo, Colorado, marine sedimentary section and their relationship to Caribbean plateau construction and oxygen anoxic event 2, *Paleoceanography*, *20*, PA3005, doi:10.1029/2004PA001093.

Sprovieri, M., N. Sabatino, N. Pelosi, S. J. Batenburg, R. Coccioni, M. Iavarone, and S. Mazzola (2013), Late Cretaceous orbitally-paced carbon isotope stratigraphy from the Bottaccione Gorge (Italy), *Palaeogeogr. Palaeoclimatol. Palaeoecol.*, *379–380*, 1–94, doi:10.1016/j.palaeo.2013.04.006.

Stoll, H. M., and D. P. Schrag (2000), High-resolution stable isotope records from the Upper Cretaceous rocks of Italy and Spain: Glacial episodes in a greenhouse planet?, *Geol. Soc. Am. Bull.*, *112*, 308–319, doi:10.1130/0016-7606(2000)112<0308:hrsirf>2.3.co;2.

Swenson, J. B. (2005), Fluviodeltaic response to sea level perturbations: Amplitude and timing of shoreline translation and coastal onlap, *J. Geophys. Res.*, *110*, F03007, doi:10.1029/2004JF000208.

Thomson, D. J. (1982), Spectrum estimation and harmonic analysis, *IEEE Proc.*, *70*, 1055–1096, doi:10.1109/PROC.1982.12433.

Tian, J., W. Ma, M. W. Lyle, and J. K. Shackford (2014), Synchronous mid-Miocene upper and deep oceanic $\delta^{13}C$ changes in the east equatorial Pacific linked to ocean cooling and ice sheet expansion, *Earth Planet. Sci. Lett.*, *406*, 72–80, doi:10.1016/j.epsl.2014.09.013.

Toggweiler, J. R. (2008), Origin of the 100,000-year timescale in Antarctic temperatures and atmospheric CO_2, *Paleoceanography*, *23*, PA2211, doi:10.1029/2006PA001405.

Trabucho Alexandre, J., E. Tuenter, G. A. Henstra, K. J. van der Zwan, R. S. W. van de Wal, H. A. Dijkstra, and P. L. de Boer (2010), The mid-Cretaceous North Atlantic nutrient trap: Black shales and OAEs, *Paleoceanography*, *25*, PA4201, doi:10.1029/2010PA001925.

Tukey, J. W. (1977), *Exploratory Data Analysis*, Addison-Wesley, Reading, Mass.

Turetsky, M. R., B. Benscoter, S. Page, G. Rein, G. R. van der Werf, and A. Watts (2015), Global vulnerability of peatlands to fire and carbon loss, *Nat. Geosci.*, *8*, 11–14, doi:10.1038/ngeo2325.

Turgeon, S. C., and R. A. Creaser (2008), Cretaceous oceanic anoxic event 2 triggered by a massive magmatic episode, *Nature*, *454*, 323–326, doi:10.1038/nature07076.

Uličný, D., I. Jarvis, D. Gröcke, S. Čech, J. Laurin, K. Olde, J. Trabucho-Alexandre, L. Švábenická, and N. Pedentchouk (2014), A high-resolution carbon-isotope record of the Turonian stage correlated to a siliciclastic basin fill: Implications for mid-Cretaceous sea-level change, *Palaeogeogr. Palaeoclimatol. Palaeoecol.*, *405*, 42–58, doi:10.1016/j.palaeo.2014.03.033.

Voigt, S., A. Aurag, F. Leis, and U. Kaplan (2007), Late Cenomanian to Middle Turonian high-resolution carbon isotope stratigraphy: New data from the Münsterland Cretaceous Basin, Germany, *Earth Planet. Sci. Lett.*, *253*, 196–210, doi:10.1016/j.epsl.2006.10.026.

von Strandmann, P. A. E. P., H. C. Jenkyns, and R. G. Woodfine (2013), Lithium isotope evidence for enhanced weathering during Oceanic Anoxic Event 2, *Nat. Geosci.*, *6*, 668–672, doi:10.1038/ngeo1875.

Walaszczyk, I., C. J. Wood, J. A. Lees, D. Peryt, S. Voigt, and F. Wiese (2010), The Salzgitter-Salder Quarry (Lower Saxony, Germany) and Słupia Nadbrzeżna river cliff section (central Poland): A proposed candidate composite Global Boundary Stratotype Section and Point for the Coniacian Stage (Upper Cretaceous), *Acta Geol. Polonica*, *60*, 445–477.

Wang, C., R. W. Scott, X. Wan, S. A. Graham, Y. Huang, P. Wang, H. Wu, W. E. Dean, and L. Zhang (2013), Late Cretaceous climate changes recorded in Eastern Asian lacustrine deposits and North American Epeiric sea strata, *Earth Sci. Rev.*, *126*, 275–299, doi:10.1016/j.earscirev.2013.08.016.

Weissert, H., A. Lini, K. B. Föllmi, and O. Kuhn (1998), Correlation of Early Cretaceous carbon isotope stratigraphy and platform drowning events: A possible link?, *Palaeogeogr. Palaeoclimatol. Palaeoecol.*, *137*, 189–203, doi:10.1016/S0031-0182(97)00109-0.

Wendler, I. (2013), A critical evaluation of carbon isotope stratigraphy and biostratigraphic implications for Late Cretaceous global correlation, *Earth Sci. Rev.*, *126*, 116–146, doi:10.1016/j.earscirev.2013.08.003.

Wendler, J. E., S. R. Meyers, I. Wendler, and J. Kuss (2014), A million-year-scale astronomical control on Late Cretaceous sea-level, *Newsl. Stratigr.*, *47*, 1–19, doi:10.1127/0078-0421/2014/0038.

Wu, H., S. Zhang, G. Jiang, L. Hinnov, T. Yang, H. Li, X. Wan, and C. Wang (2013), Astrochronology of the Early Turonian-Early Campanian terrestrial succession in the Songliao Basin, northeastern China and its implications for long-period behavior of the Solar System, *Palaeogeogr. Palaeoclimatol. Palaeoecol.*, *385*, 55–70, doi:10.1016/j.palaeo.2012.09.004.

Wunsch, C. (2010), Towards understanding the Paleocean, *Quat. Sci. Rev.*, *29*, 1960–1967, doi:10.1016/j.quascirev.2010.05.020.

Zachos, J. C., M. Pagani, L. Sloan, E. Thomas, and K. Billups (2001), Trends, rhythms, aberrations in global climate 65 Ma to present, *Science*, *292*, 686–693, doi:10.1126/science.1059412.

Zachos, J. C., G. R. Dickens, and R. E. Zeebe (2008), An early Cenozoic perspective on greenhouse warming and carbon-cycle dynamics, *Nature*, *451*, 279–283, doi:10.1038/nature06588.